IOP Publishing Smart Materials and Structures
Smart Mater. Struct. **30** (2021) 125027 (19pp) https://doi.org/10.1088/1361-665X/ac3431

Ionic polymer metal composite compression sensors with 3D-structured interfaces

Rebecca Histed[1], Justin Ngo[2], Omar A Hussain[2], Chantel K Lapins[2], Omid Fakharian[1], Kam K Leang[2], Yiliang Liao[3] and Matteo Aureli[1,*]

[1] Department of Mechanical Engineering, University of Nevada, Reno 1664 N Virginia St., Reno, NV 89557, United States of America
[2] Department of Mechanical Engineering, University of Utah 1495 E. 100 S., Salt Lake City, UT 84112, United States of America
[3] Industrial and Manufacturing Systems Engineering, Iowa State University 2529 Union Dr, Ames, IA 50011, United States of America

E-mail: maureli@unr.edu

Received 20 July 2021, revised 13 September 2021
Accepted for publication 28 October 2021
Published 12 November 2021

Abstract

In this paper, we report the development of tailored 3D-structured (engineered) polymer-metal interfaces to create enhanced 'engineered ionic polymer metal composite' (eIPMC) sensors towards soft, self-powered, high sensitivity strain sensor applications. We introduce a novel advanced additive manufacturing approach to tailor the morphology of the polymer-electrode interfaces via inkjet-printed polymer microscale features. We hypothesize that these features can promote inhomogeneous strain within the material upon the application of external pressure, responsible for improved compression sensing performance. We formalize a minimal physics-based chemoelectromechanical model to predict the linear sensor behavior of eIPMCs in both open-circuit and short-circuit sensing conditions. The model accounts for polymer-electrode interfacial topography to define the inhomogeneous mechanical response driving electrochemical transport in the eIPMC. Electrochemical experiments demonstrate improved electrochemical properties of the inkjet-printed eIPMCs as compared to the standard IPMC sensors fabricated from Nafion polymer sheets. Similarly, compression sensing results show a significant increase in sensing performance of inkjet-printed eIPMC. We also introduce two alternative methods of eIPMC fabrication for sub-millimeter features, namely filament-based fused-deposition manufacturing and stencil printing, and experimentally demonstrate their improved sensing performance. Our results demonstrate increasing voltage output associated to increasing applied mechanical pressure and enhanced performance of the proposed eIPMC sensors against traditional IPMC based compression sensors.

Keywords: ionic polymer metal composites, compression sensing, additive manufacturing, inkjet printing, stencil printing, 3D printing

(Some figures may appear in colour only in the online journal)

* Author to whom any correspondence should be addressed.

1. Introduction

Recent research efforts have emphasized the critical need for soft strain sensors for a variety of applications, spanning from bioengineering, rehabilitation and medicine, soft robotics, to human-machine interactions [1, 2]. Despite desirable soft mechanical characteristics, many current soft strain sensors often suffer from the major drawback of necessitating externally powered electric circuits, which convert the strain-induced changes of electrical impedance of the sensor into usable electrical signals. This severely limits the possibility to make such sensors light weight, comfortable to wear, and capable of functioning over long periods of time. On the other hand, existing self-powered sensors, for example piezoelectric ceramics, are typically stiff, non-stretchable, and limited to small deformations [3]. Thus, there is a clear and urgent need to identify novel material systems, including for example flexible piezoelectric or triboelectric nanogenerators [4], that combine self-powered behavior with soft mechanical characteristics for creating next generation strain sensors.

Ionic polymer metal composites (IPMCs) are smart electroactive soft composite materials that comprise a thin electrically charged polymer membrane, plated with noble metal electrodes, and infused with a charged solution [5–8]. In the sensing mode, when mechanical deformation is imposed on an IPMC strip, redistribution of the mobile ions within the membrane results in an electrical signal at the IPMC electrodes [9]. The concept of IPMC sensors is extremely attractive because of their soft nature (effective Young's modulus [10] of the order of 100 MPa), their excellent linearity with respect to imposed mechanical deformations [9], and their self-powered operation (IPMC sensors do not require batteries or external energy sources). However, most studies have focused on the feasibility of IPMCs as actuators, while only few have considered force and displacement sensors [11–14] and energy harvesting devices [10, 15–17]. Additionally, the vast majority of the sensing applications have explored exclusively bending mode systems.

The long-standing challenges of limited sensitivity [12], poor property control, and non-versatile modes of operation have so far dramatically hampered the use of IPMC sensors. Specifically, IPMCs exhibit extremely large variability in terms of their multiphysics properties (in particular, capacitance [18]). Variability and inconsistency, in turn, demand extensive property and performance characterization of each individual IPMC sample before use in any sensor system. Furthermore, until recent advancements [19–22], the limited understanding of the fundamental nature of material response to non-bending deformation in IPMCs has effectively precluded major breakthroughs in the development of non-bending mode sensors. In particular, a theoretical explanation of the compression sensing mode (electrical transduction of deformation in the thickness direction due to applied pressure normal to the electrodes) was only offered in 2017 in [22] and therein attributed to inhomogeneous strain through the IPMC thickness. Since in traditional IPMCs the inhomogeneous deformation depends on material properties that cannot be controlled by design during the fabrication process, traditional IPMC sensitivity in compression mode is typically very low (e.g. 3 μA per 1% strain deformation [22]). Therefore, this very attractive sensing mode has not so far been well explored although, very recently, the work in [23] proposes IPMCs pressure sensors with a gradient shape designed to induce stress (and strain) inhomogeneities across the sensor thickness.

This paper tackles the challenge of dramatically improving the multiphysics properties of IPMCs by, for the first time, directly engineering the role of polymer-metal interface in defining the material response. Specifically, we hypothesize that the multiphysics sensing properties of IPMCs can be significantly enhanced by tailored polymer-metal interfaces. To test this hypothesis, we introduce three advanced additive manufacturing (AAM) methods for the fabrication of a novel embodiment of IPMC sensor technology, that we name 'engineered IPMCs' (or, eIPMCs for short), namely: (a) inkjet-printed eIPMCs with microscale features at the polymer-metal interface, (b) filament-based fused-deposition manufactured (FDM 3D printed) eIPMCs, inspired by recently-developed IPMC 3D-printing fabrication process [24], and (c) stencil-printed eIPMCs, inspired by the recent results in [25]. These architectures leverage the design of electrode-polymer interface micro- and sub-millimeter-scale structures to enhance IPMC sensing performance, particularly in the compression sensing mode. Furthermore, a minimal physics-based chemo-electromechanical model that captures structure-property-performance relationships to demonstrate enhanced capacitance and strain sensing performance is proposed. The model can also be used to inform the design of engineered interfaces in eIPMC material. Thus, the contributions of this paper consist in the development of a new class of materials, that is, eIPMCs, with experimentally demonstrated superior multiphysics properties for high sensitivity strain sensor applications and in a set of validated predictive modeling tools for their multiphysics behavior. Importantly, our exploratory results demonstrate enhanced performance of the proposed sensors against traditional IPMC based compression sensors.

The rest of the paper is organized as follows. In section 2, we propose a minimal, physics-based chemoelectromechanical model to describe compression sensing in eIPMCs. In section 3, we present our novel inkjet printed eIPMC samples, describing the fabrication process, electrochemical property testing and relations with the designed microstructure, and compression sensing performance. In section 4 we propose two alternative manufacturing processes for creating eIPMC materials with sub-mm features and present their compression sensing behavior results. Some general remarks are offered in section 5 and conclusions are articulated in section 6.

2. Modeling eIPMC compression sensors

2.1. Problem statement and nomenclature

The problem under consideration is schematically depicted in figure 1, along with the relevant nomenclature. We study the chemoelectromechanical transduction via a purely one-dimensional through-the-thickness problem for an eIPMC

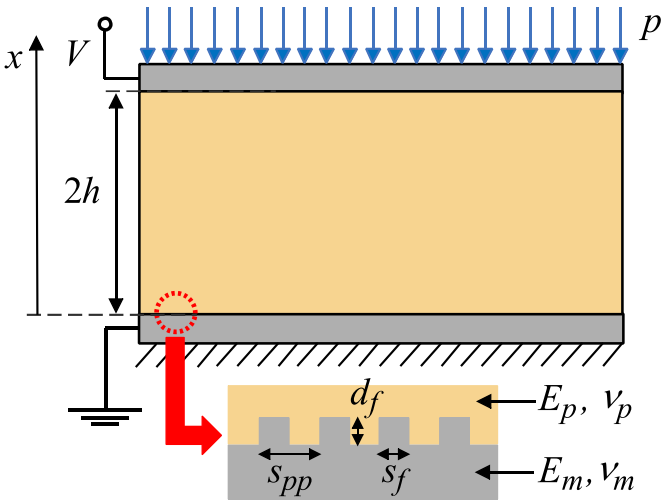

Figure 1. Schematic representation and nomenclature of the problem, with detail of the engineered interface region. Here, V is the electric potential at the movable electrode, p is the applied pressure, h is the polymer semithickness, x is the through-the-thickness coordinate. Young's modulus and Poisson's ratio are E_p and ν_p for the polymer and E_m and ν_m for the metal electrodes, respectively. Geometry of the representative engineered interface is described by polymer feature size s_f, polymer feature height d_f, and periodic spacing s_pp between features.

of semithickness h with its grounded engineered electrode at $x=0$ and its movable conventional (nominally flat) electrode at $x=2h$. For simplicity, we will consider a two-dimensional pattern in the interface of the engineered electrode, assumed to be fabricated by some additive manufacturing process on the polymer side, with given dimensions as shown in figure 1. The prototypical topography in figure 1 could represent ridges in the direction orthogonal to the page or pillar-like cylindrical structures arranged in the plane $x=0$ of the electrode. As explained later, we will forego a detailed description of the interface and will assume that the polymer-metal interface is sharp and located at $x=0$. Young's modulus and Poisson's ratio of the material are indicated with E and ν, respectively, with a subscript p or m to indicate polymer or metal, respectively. The polymer is assumed to be mechanically and electrochemically homogeneous and isotropic. We will consistently neglect the presence of steric effects [26], composite layers [27], and electrode surface roughness [18, 28]. We will also assume that the electrodes are perfectly rigid and conductive.

2.2. A minimal mechanical model

To describe the essential aspects of the eIPMC mechanical behavior, we will consider a one-dimensional plane strain compression model, upon quasi-static application of a possibly time-varying uniform pressure $p(t)$ normal to the movable electrode initially at $x=2h$. Far from the engineered electrode at $x=0$, the (engineering) stress field in the material is uniform and given by $-p$ while the (engineering) strain is given by $\epsilon_x=-p/E_\mathrm{p}\equiv-\epsilon_\mathrm{R}$ with, obviously, $\epsilon_y=0$. Here, the symbol ϵ_R is used to indicate the absolute value of the remote uniform strain p/E_p. In the vicinity of the engineered electrode, the strain field becomes significantly more complicated due to stress concentration effects and the geometric pattern on the engineered electrode. This inhomogeneous deformation developed in the eIPMC is responsible for the sensing behavior, as also pointed out in [22].

In order to capture the inhomogeneous deformation, rather than formalizing a homogenization procedure for the micromechanical properties of the engineered electrode, for example along the lines of [29], we conduct a representative finite element simulation on a simplified model to understand fundamental properties of the strain field, see figure 2. In the representative simulation, we assume linear elastic, homogeneous and isotropic behavior for metal and polymer, we set $E_\mathrm{m}=100E_\mathrm{p}$, $\nu_\mathrm{m}=0.3$, and $\nu_\mathrm{p}=0.49$, and we design a simple periodic pattern for the protrusion of the engineered electrode, with $s_\mathrm{f}=d_\mathrm{f}=s_\mathrm{pp}/2$. These values are representative, and chosen to highlight the large stiffness contrast between the polymer (essentially incompressible) and the metal phases. The hypothesis of linear elastic, homogeneous and isotropic behavior for IPMC material is common in the literature [10, 22]. We conduct a linear static plane strain analysis on a representative section of eIPMC and we determine the dilatation field $\Delta=\epsilon_x+\epsilon_y$ (or trace of the strain tensor), that is, the local relative change in volume of the polymer upon mechanical compression [10], see figure 2.

As expected, simulations show that, far from the engineered electrode, the dilatation is simply equal to the remote strain value $\Delta=\epsilon_x=-\epsilon_\mathrm{R}$. In the vicinity of the engineered electrode, on the other hand, the strain field becomes two dimensional, with $\epsilon_y\neq0$. The absolute value of the dilatation decreases over a lengthscale of the order of d_f (which can be presumed of the same order of the height of the protrusions in the electrode pattern) to a value at the electrode interface at $x=0$, whose exact magnitude may depend in a complicated way on material and geometric properties of the interface. As an example, two specific dilatation profiles are shown for two locations (highlighted by the solid and dashed cut lines in figure 2). These profiles highlight jump behavior of the dilatation at the transition between polymer and metal. To avoid the need of a description dependent on the y-coordinate, we consider quantities averaged in the y-direction over an integer number of periods of the electrode topography. These averages display a peculiar behavior which is summarized by observing that: (a) far from the electrode, $\Delta=-\epsilon_\mathrm{R}$; (b) in the polymer/metal protrusions region, Δ decreases (in absolute value) until a final value is reached in (c) the electrode bulk region, comprised of only metal.

Based on these findings, in the following we will assume that the representative y-averaged behavior of the dilatation can be sufficiently well described, in a simplified one-dimensional analysis, by the following model

$$\Delta(x,t)=-\frac{p(t)/E_\mathrm{p}}{\{1+\alpha\exp[-(x/d_\mathrm{f})^2]\}} \tag{1}$$

where now the parameter α takes on the role of a tuning parameter, in the absence of a more detailed micromechanical

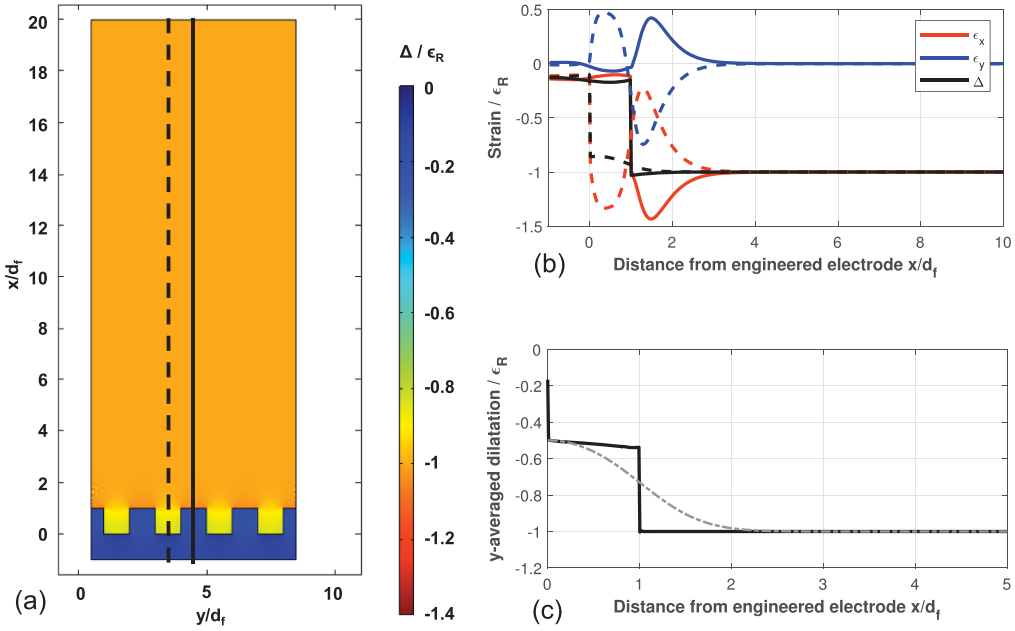

Figure 2. (a) Representative finite element results obtained in COMSOL Multiphysics software package on the dilatation Δ/ϵ_R in the eIPMC subject to uniaxial compression in the x-direction. Symmetry boundary conditions are used on the lateral faces of the model. The bottom face is fixed and a uniform vertical displacement is applied to the top face. Note that the dilatation of the electrode is essentially negligible as compared to that of the polymer. (b) Strain profiles for ϵ_x and ϵ_y and dilatation profile Δ. In (b), data shown as solid and dashed lines are taken along the solid and dashed cut lines in (a), taken through the metal and through the polymer protrusions, respectively. (c) Actual dilatation profile averaged in the y-direction (solid line) and simplified (continuous) dilatation profile (dash-dotted line).

homogenization which is outside the scope of this paper. Figure 2 shows the actual dilatation profile (solid line) compared with the one (dashed line) obtained from equation (1) with $\alpha = 1$. As explained later, the detailed form of equation (1) has only limited impact on the description of the sensing behavior, so we satisfy ourselves with the simple representation offered above. The important point to note in equation (1) is that the parameter α represents a measure of the asymmetry in the mechanical behavior of the regions in proximity of the engineered electrode and the conventional electrode. Specifically, if both electrodes were conventional and nominally flat and identical, we would have $\alpha = 0$.

It is worthwhile to remark that a different physical interpretation for equation (1) can be obtained by assuming that the polymer membrane is a material with functionally graded Young's modulus, sandwiched between flat electrodes, that follows a spatial variation described by $E_{fg}(x) = E_p\{1 + \alpha \exp[-(x/d_f)^2]\}$. Here, the deformation response under a uniform applied pressure would have a one-dimensional solution with $\epsilon_x(x,t) = -p(t)/E_{fg}(x) = \Delta(x,t)$ and $\epsilon_y = 0$. Based on this interpretation, an alternative simplified (but discontinuous) model for the eIPMC Young's modulus could be given as $E_{fg}(x) = E_c$ for $x < d_f$ and $E_{fg}(x) = E_p$ for $d_f < x < 2h$, where E_c represents a homogenized modulus of the interface which thus resembles a composite layer [27] for mechanical properties. The homogenized modulus E_c can be estimated for example via the 'inverse rule of mixtures', postulating uniform stress in the interface region, so that $E_c = [\phi/E_p + (1-\phi)/E_m]^{-1}$, where ϕ is the volume fraction of the polymer (volume of polymer per unit volume of interface) and can be in principle estimated by the interfacial topography. For example, for the minimal problem in figure 2, since $\phi = 0.5$ and $E_p \ll E_m$, we have $E_c \approx E_p/\phi$ which would lead to the (in this case, quite accurate) estimate $\Delta = -p/E_c \approx -\phi p/E_p = -0.5\,\epsilon_R$. Alternatively, tighter bounds based on the detailed shape of the interface can be proposed [30]. However, in this paper we prefer to maintain the continuous description of the dilatation field as in equation (1), rather than the piecewise continuous form that would stem from this approach, although in the following we will often discuss implications of this alternative modeling choice.

We remark that this derivation has been obtained independently of possible chemoelectromechanical coupling, effectively separating the problem in two simpler substeps, the first of which consists in determining the mechanical deformation in response to a pressure input. In what follows, we will use this local dilatation in the second substep, where the imposed mechanical deformation (and resulting dilatation) will be correlated to the chemoelectromechanical response of the eIPMC.

2.3. *Linear chemoelectromechanical sensing*

Here, we will focus on the linear response of the eIPMC compression sensor, under the hypothesis of small deformations, electric potentials, and deviations of the counterion concentration from the concentration at rest. The governing equations for IPMC chemoelectromechanical sensing behavior in the nonlinear case have been developed in [9], and further significantly enriched in [22, 31]. With specialization to the case

at hand, and following in part [32], a linearized version of the equations in [9] is given by

$$-\varepsilon_0\varepsilon_r\frac{\partial^2\,\psi(x,t)}{\partial x^2} = F\{c(x,t)-c_0[1-\Delta(x,t)]\} \tag{2a}$$

$$\frac{\partial c(x,t)}{\partial t}+c_0\,\frac{\partial\Delta(x,t)}{\partial t} = D\left[\frac{\partial^2 c(x,t)}{\partial x^2}+\frac{Fc_0}{RT}\frac{\partial^2\,\psi(x,t)}{\partial x^2}\right]. \tag{2b}$$

Equation (2*a*), consistent with the model in [10], is Poisson's equation, which establishes the relationship (Gauss' law) between the electric potential ψ and the free charge in the eIPMC, where F is Faraday's constant, c is the concentration of mobile counterions, c_0 is the concentration of fixed ions, and ε_0 and ε_r are the vacuum permittivity and the eIPMC relative permittivity, respectively, and assumed to be constant. It is important to note that the concentrations of mobile counterions and fixed ions are calculated with respect to the deformed volume of the eIPMC. Equation (2*b*) is the linearized generalized Nernst-Planck equation which establishes conservation of charge in the eIPMC. Here, D is the counterion diffusivity in the bulk polymer, R is the universal gas constant, and T is the IPMC temperature. Note that, when compared to the model reported in [10], equation (2*b*) is enriched with the important advective term $c_0\,\partial\Delta/\partial t$, see also the discussion in [32], to capture the change in concentration, even in the absence of ion flux, due to the mechanical deformation of the eIPMC. The right hand side of equation (2*b*) is also recognized as the (negative) divergence of the linearized ion flux J which is defined as $J=-D[\partial c/\partial x+(Fc_0)/(RT)\partial\psi/\partial x]$.

The governing equations are subject to appropriate boundary and initial conditions. We set here initial chemoelectromechanically neutral conditions as $p(0)=0$, $\psi(x,0)=0$, and $c(x,0)=c_0$. Boundary conditions are such that $\psi(0,t)=0$ at the grounded electrode and $\psi(2h,t)=V(t)$ at the movable electrode. The value of V will be prescribed later in the study of short-circuit (SC) or open-circuit (OC) conditions. In addition, as customary, we prescribe ion-blocking conditions at the electrodes at $x=0$ and $x=2h$, which set the ion flux to zero at the polymer-electrode interfaces, that is, $J(0,t)=J(2h,t)=0$ [32].

As in standard practice, it is convenient to nondimensionalize the governing equations and their boundary conditions by scaling all lengths and displacements with the polymer semithickness h, the time variable t with a characteristic time t_0 to be defined in the following, and the electric potential ψ with the thermal voltage $V_{\rm th}=RT/F$. In addition, it is useful to nondimensionalize the applied pressure p with the bulk Young's modulus of the polymer $E_{\rm p}$, so that $p/E_{\rm p}=\tilde{p}$, where the superimposed tilde notation indicates a nondimensional quantity. Thus, the dilatation becomes $\Delta(\tilde{x},\tilde{t})=-\tilde{p}(\tilde{t})/K(\tilde{x})$, with $K(\tilde{x})=1+\alpha\exp[-(\tilde{x}/\tilde{d}_{\rm f})^2]$. We also define the nondimensional counterion over-concentration $\tilde{\chi}(\tilde{x},\tilde{t})=[c(h\tilde{x},t_0\,\tilde{t})-c_0]/c_0$. Similarly, we define $\tilde{\psi}(\tilde{x},\tilde{t})=\psi(h\tilde{x},t_0\,\tilde{t})/V_{\rm th}$ and $\tilde{J}(\tilde{x},\tilde{t})=-\partial[\tilde{\chi}(\tilde{x},\tilde{t})+\tilde{\psi}(\tilde{x},\tilde{t})]/\partial\tilde{x}$.

With these positions, and neglecting the explicit dependence on the independent variables, the nondimensional form of equations (2*a*) and (2*b*) reads

$$-\delta^2\,\frac{\partial^2\,\tilde{\psi}}{\partial\tilde{x}^2}=\tilde{\chi}-\tilde{p}/K, \tag{3a}$$

$$\frac{\partial\tilde{\chi}}{\partial\tilde{t}}-\frac{1}{K}\frac{\partial\tilde{p}}{\partial\tilde{t}}=\delta\left[\frac{\partial^2\,\tilde{\chi}}{\partial\tilde{x}^2}+\frac{\partial^2\,\tilde{\psi}}{\partial\tilde{x}^2}\right], \tag{3b}$$

where we have also defined $\delta=\lambda_{\rm D}/h$ as the ratio between the Debye screening length $\lambda_{\rm D}=\sqrt{(\varepsilon_0\,\varepsilon_{\rm r}RT)/(f^2\,c_0)}$ and the polymer semithickness h. Similarly, nondimensional boundary conditions are $\tilde{\psi}(0,\tilde{t})=0$, $\tilde{\psi}(2,\tilde{t})=\tilde{V}(\tilde{t})$, with $\tilde{V}(\tilde{t})=V(t_0\,\tilde{t})/V_{\rm th}$, and $\tilde{J}(0,\tilde{t})=\tilde{J}(2,\tilde{t})=0$. In the derivation of equation (3*b*), we let the characteristic time $t_0=(\lambda_{\rm D}h)/D$, that is, the diffusion timescale within the charge boundary layers [28]. Note that this timescale will allow us to conveniently separate the evolution of the mechanical phenomena from that of the electrochemical phenomena and, from a physical perspective, corresponds to considering mechanical deformations significantly slower than the typical electrochemical timescales, which is of the order of milliseconds [28]. Note that the form of the presented equations and boundary conditions is slightly different from that used in [22], as the concentrations therein are expressed per unit undeformed volume.

It is important to note that, in practical IPMC and eIPMC applications, $\lambda_{\rm D}\approx 10^{-10}$ m and the parameter δ is thus of the order of 10^{-6} [33]. Therefore, equations (3*a*) and (3*b*) describe a singularly perturbed system whose solution is best attacked by way of matched asymptotic expansions [34]. We will sketch below the solution procedure, which follows the steps in [22, 33]. In the rest of the derivation, we will drop the superscript tilde for notational convenience although we will consistently refer to nondimensional variables, except where explicitly noted. We will also use a superimposed dot notation to indicate time derivatives and a prime notation to indicate spatial derivatives.

2.4. Matched asymptotic expansions

We consider a bulk zone in which an outer expansion is sought, and two boundary layer zones, in proximity of the polymer-metal interfaces, where inner expansions are sought. The idea is sketched in figure 3 and the relevant governing equations are developed in the following.

2.4.1. Outer expansion. In the eIPMC bulk, we consider a regular asymptotic expansion of χ and ψ in terms of the small parameter δ, such that $\chi^{(B)}=\chi_0^{(B)}+\delta\chi_1^{(B)}+\delta^2\,\chi_2^{(B)}+\ldots$ and $\psi^{(B)}=\psi_0^{(B)}+\delta\psi_1^{(B)}+\delta^2\,\psi_2^{(B)}+\ldots$, where the symbol (B) indicates the outer expansion in the bulk. Substituting these representations in equations (3*a*), and approximating the outer solution with its leading order term of $\mathcal{O}(\delta^0)$, we obtain

$$\chi^{(B)}\approx\chi_0^{(B)}=p/K(x) \tag{4a}$$

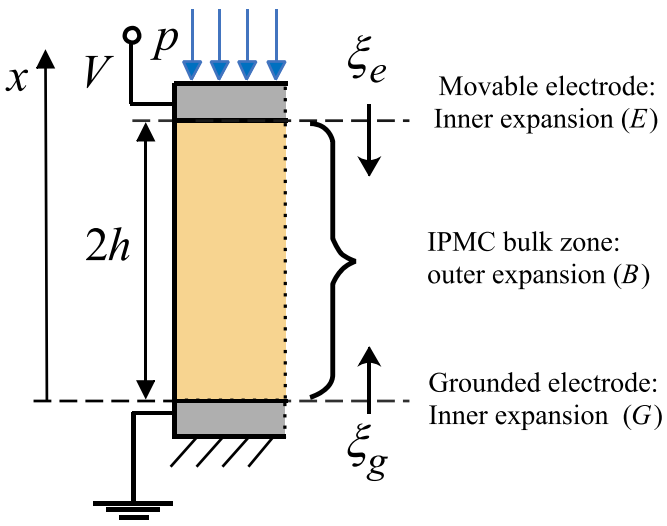

Figure 3. Schematic representation of the strategy of matched asymptotic expansions, with labels indicating the three expansion zones.

$$\psi^{(B)} \approx \psi_0^{(B)} = -p/K(x) + A_1^{(B)}(t)x + A_0^{(B)}(t) \qquad (4b)$$

where $A_1^{(B)}(t)$ and $A_0^{(B)}(t)$ are yet unknown integration parameters, functions of time.

2.4.2. Inner expansion at the grounded electrode. In the vicinity of the grounded electrode at $x=0$, we magnify the spatial coordinate by introducing the stretched variable $\xi_g = x/\delta$, where the subscript g stands for grounded electrode. We perform the change of variables in equation (3*a*) and seek a regular asymptotic expansion of χ and ψ in the boundary layer region in terms of the small parameter δ, such that $\chi^{(G)} = \chi_0^{(G)} + \delta\chi_1^{(G)} + \delta^2\ \chi_2^{(G)} + \ldots$ and $\psi^{(G)} = \psi_0^{(G)} + \delta\psi_1^{(G)} + \delta^2\ \psi_2^{(G)} + \ldots$, where the symbol (G) indicates the inner expansion in the boundary layer at the grounded electrode. Thus, at the leading order, equations (3*a*) and (3*b*) reduce to $\chi_0^{(G)} + (\psi_0^{(G)})'' = p/K(0)$ and $(\chi_0^{(G)} + \psi_0^{(G)})'' = 0$, and by approximating $\chi^{(G)}$ and $\psi^{(G)}$ with their $\mathcal{O}(\delta^0)$ terms, we obtain

$$\chi^{(G)} = p/K(0) + C_2^{(G)}(t)\mathrm{e}^{-\xi_g}, \qquad (5a)$$

$$\psi^{(G)} = -p/K(0) - C_2^{(G)}(t)\mathrm{e}^{-\xi_g} + A_0^{(G)}(t), \qquad (5b)$$

where $A_0^{(G)}(t)$ and $C_2^{(G)}(t)$ are yet unknown integration parameters, functions of time. In the derivation of equations (5*a*) and (5*b*), we have also used the fact that these solutions must be bounded as $\xi_g \to \infty$, thus effectively determining the null values of the integration constants in the diverging terms $C_1^{(G)}(t)\mathrm{e}^{\xi_g}$ and $A_1^{(G)}(t)\xi_g$ of the solution.

2.4.3. Inner expansion at the movable electrode. In the vicinity of the movable electrode at $x=2$, we magnify the spatial coordinate by introducing the stretched variable $\xi_e = (2-x)/\delta$, where the subscript e stands for movable electrode. We perform the change of variables in equations (3*a*) and (3*b*) and seek a regular asymptotic expansion of χ and ψ in the boundary layer region in terms of the small parameter δ, such that $\chi^{(E)} = \chi_0^{(E)} + \delta\chi_1^{(E)} + \delta^2\ \chi_2^{(E)} + \ldots$ and $\psi^{(E)} = \psi_0^{(E)} + \delta\psi_1^{(E)} + \delta^2\ \psi_2^{(E)} + \ldots$, where the symbol (E) indicates the inner expansion in the boundary layer at the movable electrode. By closely following the steps above, we obtain

$$\chi^{(E)} = p/K(2) + C_2^{(E)}(t)\mathrm{e}^{-\xi_e}, \qquad (6a)$$

$$\psi^{(E)} = -p/K(2) - C_2^{(E)}(t)\mathrm{e}^{-\xi_e} + A_0^{(E)}(t), \qquad (6b)$$

where $A_0^{(E)}(t)$ and $C_2^{(E)}(t)$ are yet unknown functions of time and, as above, we have enforced boundedness of solutions at $\xi_e \to \infty$.

2.4.4. Matching. The inner and outer expansions determined above must be matched in such a way they share a common limit in their overlap regions [34] so that, in particular, $\lim_{x\to 0}\psi^{(B)} = \lim_{\xi_g\to\infty}\psi^{(G)}$ and $\lim_{x\to 2}\psi^{(B)} = \lim_{\xi_e\to\infty}\psi^{(E)}$, and similarly for the over-concentration solutions. These conditions yield immediately $A_0^{(B)}(t) = A_0^{(G)}(t)$ and $A_0^{(B)}(t) + 2A_1^{(B)}(t) = A_0^{(E)}(t)$.

The next matching condition pertains to continuity of the ion flux and can be enforced through the process devised in [33]. Summarizing the procedure, by integrating equation (3*b*) from the electrode to an arbitrary location in the polymer bulk, enforcing the ion-blocking condition at the interface, specializing the left-hand side to the inner solution and the right-hand side to the outer solution, and considering only the leading order of the solution, the matching yields

$$\dot{C}_2^{(G)}(t) = A_1^{(B)}(t) = -\dot{C}_2^{(E)}(t). \qquad (7)$$

Finally, the last matching condition stems from enforcing the voltage boundary conditions at the electrodes on the inner solutions. These are

$$\psi^{(G)}(\xi_g = 0) = -p/K(0) - C_2^{(G)}(t) + A_0^{(G)}(t) = 0, \qquad (8a)$$

$$\psi^{(E)}(\xi_e = 0) = -p/K(2) - C_2^{(E)}(t) + A_0^{(E)}(t) = V. \qquad (8b)$$

We now combine together the matching conditions and equations (8*a*) and (8*b*), and take a Laplace transform of equation (7), using a hat to indicate transformed quantities and letting s the Laplace variable. Then, we obtain the following linear system for $\hat{A}_1^{(B)}$ and $\hat{A}_0^{(B)}$

$$\begin{cases} (-s^{-1})\hat{A}_1^{(B)} + \hat{A}_0^{(B)} = p/K(0) \\ (2+s^{-1})\hat{A}_1^{(B)} + \hat{A}_0^{(B)} = p/K(2) + V. \end{cases} \qquad (9)$$

Solution of the linear system, conveniently performed via Cramer's rule, completes the determination of the unknown integration constants $\hat{A}_1^{(B)}$ and $\hat{A}_0^{(B)}$, that is,

$$\hat{A}_1^{(B)} = \frac{s}{2(s+1)}\hat{V} + \frac{s[1/K(2) - 1/K(0)]}{2(s+1)}\hat{p}, \qquad (10a)$$

$$\hat{A}_0^{(B)} = \frac{1}{2(s+1)}\hat{V} + \frac{K(0)+K(2)[1+2s]}{2K(0)K(2)(s+1)}\hat{p}, \qquad (10b)$$

from which the other constants can be directly determined, if desired. For ease of notation, we denote with $\gamma = [1/K(2) - 1/K(0)] = \alpha/(1+\alpha)$ which represents a measure of the asymmetry of the mechanical properties of the eIPMC in the vicinity of the grounded electrode (the engineered electrode) and the movable electrode (the conventional electrode). In particular, $0 \leqslant \gamma \leqslant 1$ and note that, if the two interfacial regions are nominally identical with no asymmetry, then $\gamma = 0$ and the term $\hat{p}$ disappears from $\hat{A}_1^{(B)}$.

2.4.5. Sensor behavior. Rather than providing the composite solution for the fields ψ and χ throughout the eIPMC domain, we opt to characterize the eIPMC sensor behavior by calculating the eIPMC current output (per unit nominal surface area) associated to the mechanical deformation and the electrochemical response. To this aim, we first calculate the charge storage at the electrodes as the jump of the electric displacement at the polymer-metal interfaces, that is, $\hat{q} = \hat{\psi}'(0) = -\hat{\psi}'(2)$, see also [10]. Specializing this expression at the grounded electrode, we have $\hat{q} = \hat{C}_2^{(G)}$. From equation (7), it is thus evident that the eIPMC current, being equal to the time derivative of the charge, is given by $\hat{A}_1^{(B)}$ so that, in summary

$$\hat{I} = \frac{s}{2(s+1)}\hat{V} + \frac{s\gamma}{2(s+1)}\hat{p} = Y(s)\hat{V} + G(s)\hat{p}, \qquad (11)$$

with obvious meaning of the symbols $Y(s)$ and $G(s)$. Equation (11) is thus our main modeling result, demonstrating that the current output of the eIPMC depends through an admittance on the voltage across its electrodes, and the mechanical deformation behaves as a voltage generator [10].

It is instructive to give equation (11) a physical interpretation in terms of an equivalent electric circuit with lumped parameters. Specifically, by dividing equation (11) through by $Y(s)$, and letting $Z(s) = 1/Y(s) = (2 + 2/s)$ as the (nondimensional) impedance of the eIPMC, equation (11) becomes

$$\hat{V} = Z(s)\hat{I} - \gamma\hat{p}, \qquad (12)$$

which represents the governing equation for the equivalent lumped circuit in figure 4. It should be noted that the impedance $Z(s)$ of the eIPMC comprises the series arrangement of one resistor (of nondimensional resistance $\mathsf{R} = 2$) and two capacitors (each of nondimensional capacitance $\mathsf{C} = 1$) modeling diffusion through the bulk thickness of the polymer and capacitive effects due to charge double layers at the polymer-electrode interfaces, respectively.

We can thus distinguish two principal operating modes for the eIPMC compression sensor: the open-circuit (OC) voltage sensing mode and the short-circuit (SC) current sensing mode. In the OC voltage sensing mode, the circuit is open and therefore $\hat{I} = 0$. Thus, the voltage across the eIPMC electrodes upon application of normal pressure is given by

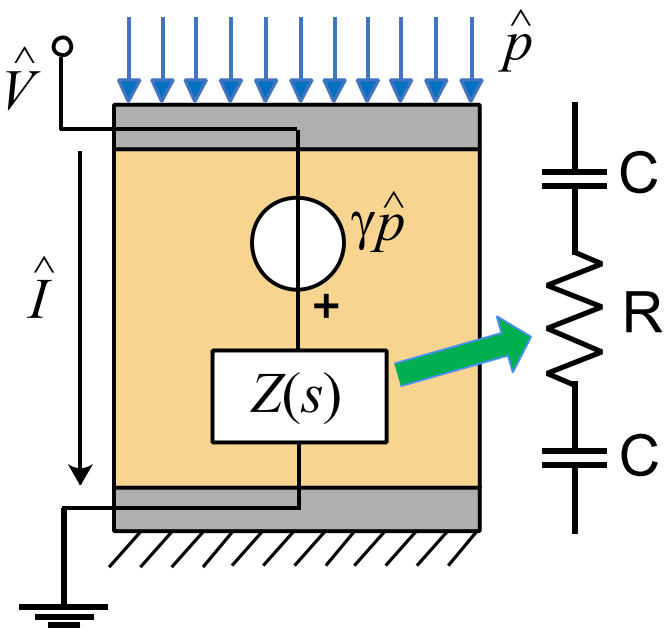

Figure 4. Equivalent lumped parameter circuit of the eIPMC compression sensor.

$$\hat{V}_{\mathrm{OC}} = -\frac{G(s)}{Y(s)}\hat{p} = -\gamma\hat{p}. \qquad (13)$$

Note that, at the timescale of the analysis of this paper, the eIPMC OC voltage output instantaneously follows the mechanical input. This is consistent with what observed for example in [9]. Importantly, if no mechanical asymmetry is present in the eIPMC, $\gamma = 0$ and no voltage is observed upon application of the mechanical pressure, see also [22]. Conversely, in the SC current sensing mode, the electrodes of the eIPMC are shorted and therefore $\hat{V} = 0$. Thus, the current through the eIPMC upon application of normal pressure is given by

$$\hat{I}_{\mathrm{SC}} = G(s)\hat{p} = \frac{\gamma s}{2(s+1)}\hat{p}. \qquad (14)$$

Note that, differently from the OC voltage, the SC current response depends on the rate of change of the applied pressure (via the term $s\hat{p}$) and its dynamics is mediated by the time constant of the RC equivalent circuit. It is illustrative to consider the response to a step input pressure, for which $\hat{p} = p_0/s$, with p_0 the magnitude of the step input (normalized by E_{p}). In this case, the nondimensional time domain response of the current is given by $I_{\mathrm{SC}}(t) = (\gamma p_0/2)\mathrm{e}^{-t}$. Once again, if no mechanical asymmetry is present in the eIPMC, no current transient is observed upon application of the mechanical pressure.

2.4.6. Observations on the role of the parameter γ. For the problem at hand, if we were to revert to the discontinuous functionally graded material description mentioned in section 2.2, the parameter γ could be alternatively estimated as $\gamma = 1 - [\phi + (E_{\mathrm{p}}/E_{\mathrm{m}})(1-\phi)]$, whose closed-form expression depends on the contrast between the polymer and metal elastic moduli and the volume fraction in the interfacial region. Again, if $E_{\mathrm{p}} \ll E_{\mathrm{m}}$, $\gamma \approx 1 - \phi$. Interestingly, this connection

allows us to estimate the tuning parameter α in the dilatation model in equation (1) from the polymer volume fraction at the interface and vice versa. Indeed, observing that $\alpha/(1+\alpha) = 1-\phi$, we have $\alpha = (1-\phi)/\phi$ and $\phi = 1/(1+\alpha)$, both in agreement with figure 2 which showed $\alpha = 1$ and $\phi = 1/2$.

Finally, this equivalence shows that a physical meaning for the tuning parameter α can be sought in the ratio of the volumes of metal and polymer at the interface and, under the simplifying assumptions discussed above, γ is well approximated by the metal volume fraction at the interface. Although motivated by a two-dimensional, plane strain reasoning and under significant simplifications (including, in particular, the uniform stress hypothesis which is overly simplistic), this analysis suggests that a design guideline for eIPMC compression sensors for optimization of the mechano-electrochemical transduction should entail the fabrication of a metal-rich interface, that maximizes the presence of metal rather than polymer, and thus maximizes $1-\phi \approx \gamma$. This could be achieved, for example, by introducing relatively small-sized polymer features on one side the surface of the polymer membrane or by synthesizing porous metal electrodes with deep, thin polymer protrusions.

These modeling results will be examined in the context of mechanical compression sensing experiments performed on eIPMCs in what follows.

3. Experimental study of eIPMC compression sensors with microscale features

3.1. Microscale feature fabrication for eIPMCs

Sample eIPMC sensors with microfeatures in the nominal form of micrometer-scale dots were created by printing microfeatures on stock N117 Nafion Membrane (procured from Ion Power, Inc.) from a FUJIFILM DMP-2850 Dimatix Materials Inkjet Printer using a specially designed ink consisting of 5% weight D521 alcohol-based Nafion dispersion and propyl alcohol, see figure 5(a). The ink concentration of 1:19 (vol/vol) was optimized based on the required surface tension (28–42 g s^{-2}) and viscosity (10–12 mPa · s) parameters of the 1 pL and 10 pL print cartridges, as per the equipment manufacturer. Before printing, the Nafion substrate was tightly secured to an acrylic plate using 3 M adhesive tape and placed inside the printer chamber. The microfeature droplets were then deposited using a custom print file that controlled the droplet formation from the piezoelectric cartridge nozzles by adjusting the nozzle voltage, jetting frequency, and waveform program. Multiple passes were employed to achieve the desired height of the microfeatures in a layer-by-layer fashion. Three different samples were successfully fabricated and will be referenced in the following as Inkjet Samples A, C, and F. Geometric properties of the pattern of the microfeatures printed on these samples are collected in table 1. Unfortunately, a complete parametric design of experiments, in which the three parameters were independently varied, was not possible due to difficulty in the fabrication process.

Figure 5(b) shows a sample of the Nafion membrane with printed micro-scale dots for the representative Sample A.

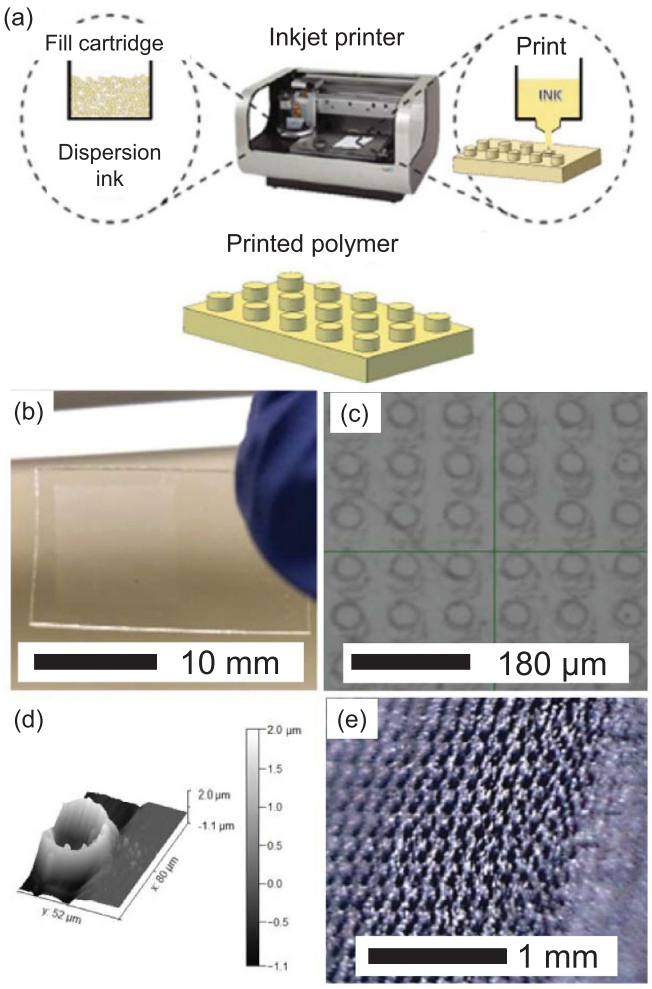

Figure 5. Sample A eIPMCs fabricated using inkjet printing technology: (a) inkjet printing process; (b) Nafion membrane with features printed onto the surface; (c) close-up view of the printed Nafion dots with spacing between 87–92 μm and dot diameter between 43–51 μm and height of approximately 2 μm; (d) AFM image of printed dot showing approximate dimensions; and (e) close-up view of plated surface of eIPMC. An upper bound for the polymer volume fraction at the interface is $\phi < 0.2$.

Table 1. Parameters of the geometric pattern of the microfeatures on the inkjet samples. Dimensions are nominal in μm.

Sample	Feature spacing	Feature diameter	Print layers
A	90	43–51	20
C	90	37	40
F	120	38–39	12

Close-up view of the dots is shown in figure 5(c), demonstrating generally consistent Nafion dots with spacing between 87 and 92 μm, dot diameter between 43–51 μm, and height of approximately 2 μm. To ensure that the inkjet-printed microfeatures adhered to the Nafion substrate, a peel test was administered using standard 3 M Scotch tape. The tape was applied and pressed onto the surface of a Nafion membrane with printed microfeatures. The tape was then peeled at a 90-degree angle in line with standard peel test protocol. After removal,

the membrane and tape were inspected under an optical microscope and the inkjet-printed microfeatures appeared intact on the membrane without any obvious residue transferred to the adhesive membrane. Figure 5(d) shows an AFM image of a printed dot, demonstrating accumulation of polymer material on the boundaries of the dot, similar to coffee-ring effect often observed in inkjet printing processes [35].

After completion and verification of the printing stage, multiple layers (up to 3) of platinum material are deposited on the surface of the printed membrane to create electrodes through the electroless plating process, using standard techniques (electroless chemical reduction, ECR) for plating platinum electrodes as described for example in [36]. The two-point resistance method was employed to check for sufficient conductivity of the electrode surface [24]. Importantly, a close-up view of the plated surface is shown in figure 5(e), from which it can be seen that the microfeatures are preserved after the electroding process.

The control (standard) IPMC compression sensors were fabricated from commercially-available Nafion sheet stock (Ion Power, Inc. membrane N117) using ECR for plating platinum electrodes as described in [36]. The control IPMC and eIPMC samples all underwent the same electroding process in the same chemical batches. This approach was incorporated to ensure that all samples were nominally exposed to the same chemical process to help mitigate impacts of the low repeatability nature of the ECR process. All fabricated IPMCs and eIPMCs were later subject to the ion exchange process and tested in their Li^+ form.

3.2. Electrochemical testing

Electrochemical characterization was performed to better understand the connection between the eIPMC microstructure and interfacial topography and the properties of the material. The tests were performed on the plated eIPMC samples to evaluate the effective impedance via potentiostatic impedance spectroscopy (EIS), double layer capacitance via cyclic voltammetry (CV), and charge–discharge behavior via chronoamperometry (CA) step response testing, see [18, 27, 37].

Prior to testing, each sample was cut to 10×10 mm^2 dimensions and adhesive copper tape was firmly attached to each eIPMC surface electrode. The test was performed under both 'dry' and 'wet' conditions. The 'dry' tests were performed with the samples resting in air after immediate removal from DI water submersion. The 'wet' condition tests were performed with the eIPMC fully submerged in DI water after allowing 30 min of preliminary submersion to ensure complete saturation of the polymer membrane. For each test, the eIPMC surface with the printed microfeatures was connected to the ground terminal of the potentiostat unit. The measurement chain is very similar to the one used in [27], except for the use of copper tape electrodes, instead of gold ones, which also prevent compression to be applied to the sample. In all electrochemical tests, a Gamry Interface 1000 potentiostat was used.

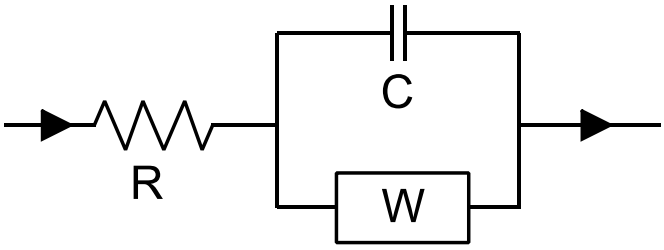

Figure 6. Equivalent circuit model for fitting impedance spectroscopy results [27].

For the chronoamperometry step response test, used to measure sample charge and discharge behavior, the step input voltage was set to 10 mV and the sampling period was 0.001 s. For the electrochemical impedance spectroscopy (EIS) test, used to measure the samples' effective impedance, the excitation AC voltage was set to 10 mV rms, that is well below the thermal voltage, approximately 25 mV. The range between 0.01 Hz and 1000 Hz was explored, with 20 points/decade. An initial delay of 100 s was used to ensure electroneutrality of the sensor. For each cyclic voltammetry (CV) test, used to measure the samples' double layer capacitance [24], the minimum and maximum voltage were set to 0.5 V and the scan rate was set to 50 mV s^{-1}.

For each EIS test, an equivalent circuit model was used to fit the eIPMC impedance spectroscopy results, see figure 6. The circuit consists of a resistor connected in series to a parallel capacitor and Warburg impedance element connection [27]. Note that our chemoelectromechanical model does not feature electrochemical composite layers and thus cannot capture the Warburg impedance effects which are however present in IPMC electrochemistry [38]. Identification of the model parameters uses the built-in routines in the Gamry potentiostat software.

Representative electrochemical testing results for the representative eIPMC sample A and control sample in dry and wet conditions are displayed in figure 7. A summary of collected test data including the eIPMC capacitance, resistance, Warburg impedance (as measured via EIS), double layer capacitance (as measured via CV), minimum and maximum peak current, and discharge time (as measured via CA) for both wet and dry testing conditions are synoptically presented in table 2. For brevity, dry test results are reported only for the control sample and inkjet sample A. Based on the results presented in figure 7 and table 2, it can be determined from the EIS results, that capacitance values for the eIPMC samples are much larger than those of the control, thus supporting the hypothesis that microengineered interfaces have the potential to improve IPMC sensing (and, possibly, actuation) performance. Inkjet sample A showed increased capacitance of 55.63% and 132.67% in dry and wet conditions, respectively. Surprisingly, the resistance of Sample A measured via EIS increases between the dry and the wet case. This behavior is not consistent with what observed in the control sample and is contrary to other findings in the literature, see for example [39]. While we do not have a definite explanation

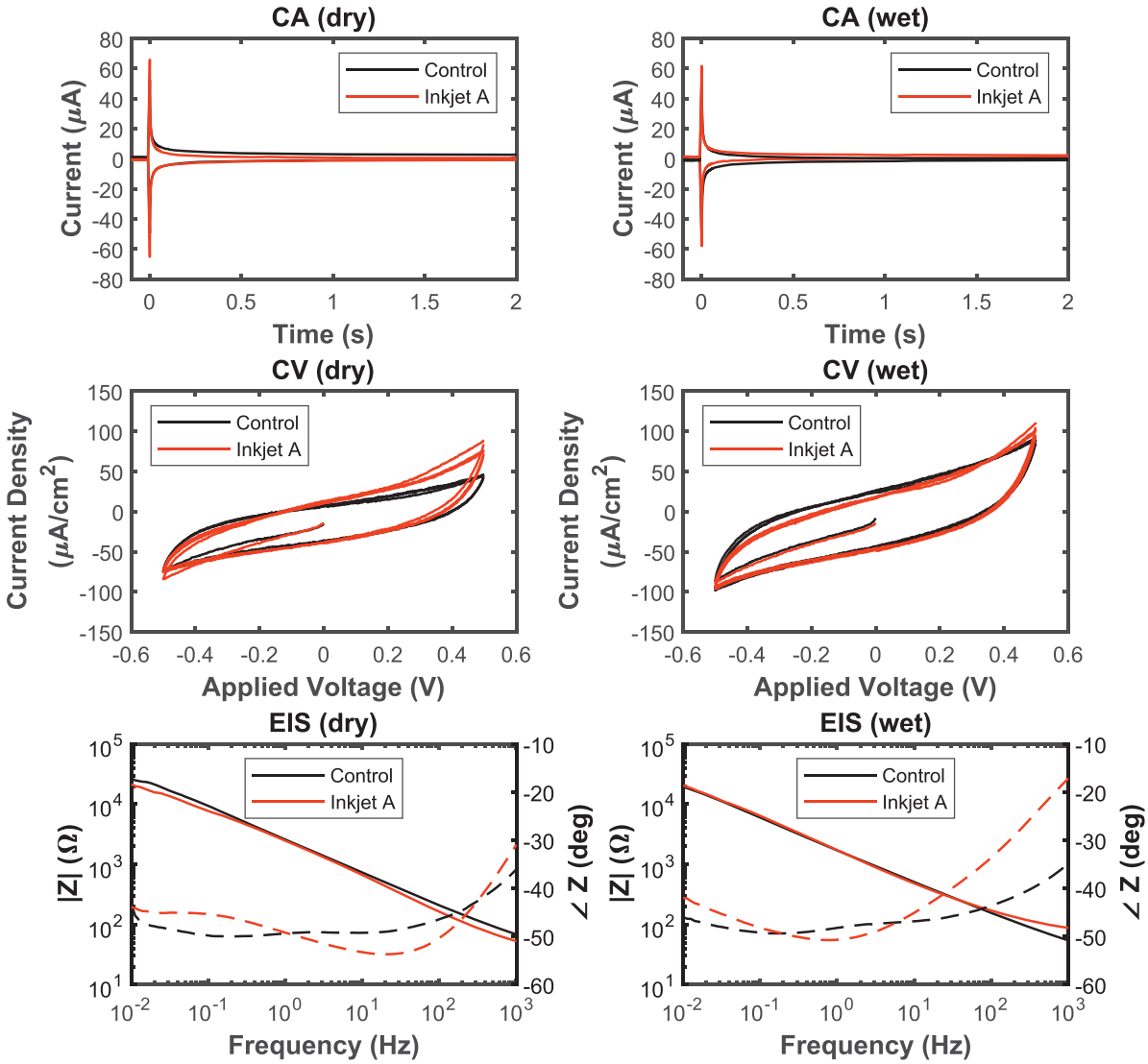

Figure 7. Electrochemical testing results of control and inkjet printing samples in dry and wet test conditions. In the EIS panels, $|Z|$ and $\angle Z$ indicate magnitude and phase of the impedance, respectively.

for this behavior, we believe that the anomalous result could be attributed either to experimental error in the hydrating process or, likely, to an imperfect fit of the EIS results to the idealized circuit model.

The inkjet-printed samples also showed significant improvements in terms of peak current, discharge time, and double layer capacitance. Specifically, sample C and sample F show the largest increase in double layer capacitance, as determined from CV, against the control in wet conditions and inkjet sample F exhibits the largest discharge time (as per CA), Warburg impedance, and smallest resistance. Note that sample C is patterned with 40 print layers which arguably lead to taller microscale features, while sample F has shallow and well-spaced features, which should promote larger metal volume fraction at the interface. It is interesting to notice that the through-the-thickness resistance of sample F is very close to that of the control sample while sample A exhibits high resistance. We can interpret this result by observing that, according to previous studies including [9, 22, 28], through-the-thickness resistance is related to the polymer thickness and not influenced by polymer-metal interfacial characteristics. As sample F has less deposited layers and smaller and widely spaced polymer protrusions, all these factors consistently contribute to comparatively smaller resistance than sample A.

3.3. Mechano-electrochemical transduction: open-circuit voltage

The sensor characterization apparatus shown in figure 8(a) is used to apply pressure to the faces of IPMC and eIPMC sensors and to measure the open-circuit voltage response, as schematically reported in figure 8(b). The apparatus consists of a stepper motor that is controlled to actuate a plate to apply pressure. A CALT DYLY-103 5KG load cell measures the load for pressure control. The applied pressure is calculated from the measured applied load and the surface area of the sample.

Table 2. Summary of electrochemical data of control sample and inkjet printing samples in dry and wet test conditions. Dry test conditions are reported for control and sample A only. EIS, CV, and CA indicate electrochemical impedance spectroscopy, cyclic voltammetry, and chronoamperometry techniques, respectively. Capacitance, resistance, and Warburg impedance from EIS measurements are indicated with C, R, and W, respectively. Double layer capacitance identified with CV is indicated with C_{dl} and calculated according to $C_{dl} = (|j^+| + |j^-|)/[2(dV/dt)]$, see [24], with j^+ and j^- the current densities at 0 V and (dV/dt) the scan rate.

	EIS				CV		CA	
Sample	C (μF)	% change (—)	R (Ω)	W ($\mu S \cdot s^{1/2}$)	Current density (min)/(max) ($\mu A\ cm^2$)	C_{dl} ($mF\ cm^{-2}$)	Peak I (+)/(−) (μA)	Discharge time (+)/(−) (ms)
Control (Dry)	3.48	—	51.07	147	−74.83/46.45	0.46	52.12/−49.35	7.39 / 6.34
Inkjet A (Dry)	5.41	55.63	43.02	162	−72.3/74.69	0.49	65.88/−65.11	4.48/4.53
Control (Wet)	3.62	—	37.97	223	−98.29/90.31	0.72	56.66/−57.55	5.67/6.16
Inkjet A (Wet)	8.43	132.67	90.32	214	−92.26/100	0.66	61.67/−57.88	4.39 / 3.81
Inkjet C (Wet)	9.26	155.41	112.5	270	−152.6/136.3	1.07	103.0/−104.0	4.23/4.40
Inkjet F (Wet)	5.09	40.40	45.02	310	−168.5/154.6	1.17	117.9/−112.1	8.47/7.23

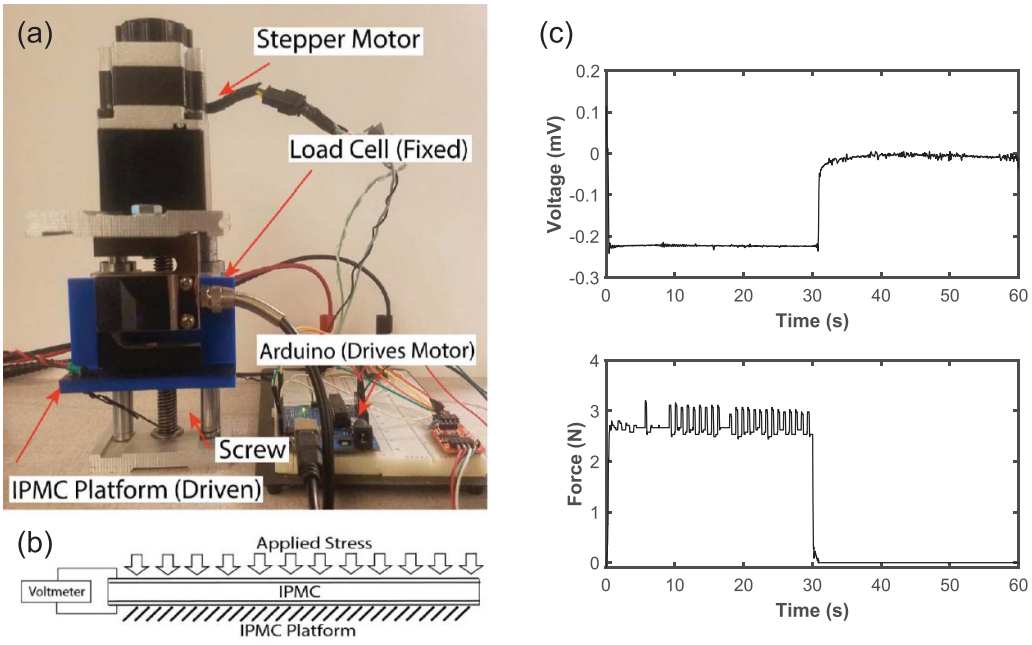

Figure 8. (a) Experimental setup for measuring open-circuit voltage of fabricated IPMC and eIPMC samples. (b) Experimental configuration for measuring open-circuit voltage of test samples. (c) Representative time history of an open-circuit voltage sensing test on inkjet sample A.

Prior to testing, each sample is fully hydrated in DI water. The step load is applied to the eIPMC sensor and held until decompression is initiated after 30 s. The total duration of each test is 60 s and the open-circuit voltage and the mechanical step response are recorded for each sample. A representative time history for an open-circuit voltage sensing test is presented in figure 8(c). The data acquisition is performed by sending the output of the load cell through an INA126 based instrumentation amplifier circuit to create an analog signal. This signal is then read into a computer using an analog-to-digital card with Simulink Real-Time.

The results for the measured normalized open-circuit voltage $V_{OC}/(RT/F)$ plotted against the normalized applied pressure p/E_p for the inkjet-printed eIPMC sensor and its control sample are shown in figure 9. All test results presented here display only the steady-state response of the system. As in the model above, the open-circuit voltage is normalized by the thermal voltage $V_{th} = RT/F \approx 25.4$ mV at room temperature,

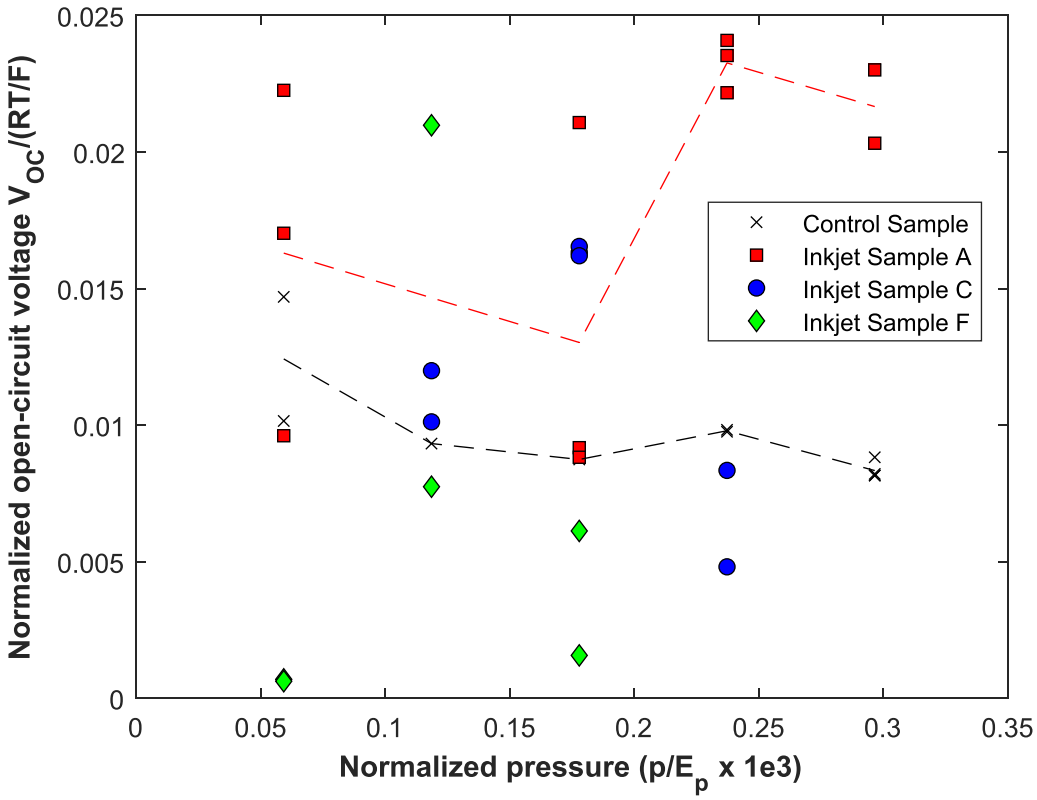

Figure 9. Measured normalized open-circuit voltage plotted against the normalized applied pressure for inkjet printed eIPMC sensors and control sample. The black and red dashed lines pass through average values for control and inkjet sample A, respectively, and are only meant to guide the eye.

and the pressure is normalized by the polymer Young's modulus which is taken as $E_p = 150$ MPa, see for example [40]. This choice is not crucial as it is only a normalization parameter in this study.

As the results show in figure 9, enhancement in sensing open-circuit voltage can be observed between the control and eIPMC sensor from inkjet sample A. Results show that for eIPMC sensor the open-circuit voltage generally increases with increased pressure. Scatter in the data does not show a strong linear trend as it would be expected from the predictions of the proposed model and equation (13). Large scatter in the data is observed for inkjet samples C and F, and no conclusion can be drawn on the behavior of these samples. For Sample C, a sharp drop in the response appears at a normalized pressure of approximately 0.25×10^{-3}. This may possibly indicate early damage in the relatively tall microfeatures of this particular sample due to severe stress concentration. For Sample F, the erratic response may be due to insufficient presence of microfeatures which, as compared to Sample A, are shorter and less densely packed.

As compared to inkjet sample A, the voltage output of the standard IPMC sensor is significantly smaller for any value of the applied pressure. Results do not display a clear trend and the response is inconclusive. We emphasize again that, in order to minimize as much as possible the impact of the electrode fabrication on the performance of control IPMC and microscale inkjet printed eIPMC, the control and the eIPMC sample are simultaneously fabricated from a single Nafion membrane, which is only patterned in part as in figure 5(b), and is later cut to separate the control and the eIPMC sample after the electroding process. Given the particular shape of the polymer protrusions resulting from the inkjet printing process (see figure 5(d)), the actual deformation process upon application of the pressure may differ significantly from the minimal model of our finite element analysis. Nevertheless, the response of the inkjet printed eIPMC sample A is consistently higher than the control experiments, on the order of $+50\%$–150%.

Experiments were conducted until $p/E_p \approx 10^{-3}$, or $p \approx 150$ kPa, but all the samples suffered damage during the compression and displayed erratic voltage response behavior. Thus, data beyond $p/E_p \approx 0.35 \times 10^{-3}$, at which point onset of damage is observed, are not reported. In figure 9 we also do not report compression data that, from the experimentally recorded voltage versus force time history, failed to yield an appreciable change in the voltage time history. We also comment that erratic behavior and these outliers may be dependent on the challenging experimental compression conditions. In particular, these may be caused by false contacts, damage to the microscale features or electrode, or otherwise changing mechanical or electrical contact conditions.

4. Fabrication, characterization, and compression experiments for eIPMC sensors with sub-mm features

4.1. Fused deposition modeling (FDM) 3D printed eIPMCs

Fused deposition modeling (FDM) 3D-printed eIPMC samples were created using the technique developed originally in [24], where a LulzBotTAZ6 3D printer was modified to print the custom-made Nafion precursor filament. Figure 10(a) shows the 3D printer, and figure 10(b) shows an illustration of the basic structure of 3D-printed eIPMC sensors with 3D-printed polymer membrane sandwiched between two platinum metal electrodes. The 3D-printing process to create the eIPMC samples first starts with creating a solid computer model with desired features. Next, the solid model is sent to the 3D printer to print the desired shape of the eIPMC sensor using ionomeric precursor filament material, layer by layer. Afterwards, the manufactured precursor structure is chemically 'activated' [24]. This process involves hydrolyzing the precursor filament in an aqueous solution of potassium hydroxide (KOH) and dimethyl sulfoxide (DMSO, C_2H_6OS). Afterwards, the eIPMC Nafion membrane was plated with platinum metal electrodes using the sample process described for the control and inkjet-printed samples. Two eIPMC samples each with different surface textures were created as shown in figure 10(c). Interestingly, the ridges fabricated on the Nafion surface bear resemblance to the two dimensional pattern examined in the proposed minimal mechanical model.

Control (standard) IPMC sensors for this study are fabricated from commercially-available Nafion sheet stock as described above. The control sensors have smooth surfaces, and one is shown in figure 10(c) with thickness of approximately 200 μm, which is approximately 40% of the thickness of the 3D printed eIPMCs. This difference is not expected to affect the comparison of the open-circuit voltage response. Importantly, note that the control sample in figure 10 is different than the control sample in figure 9 and are fabricated in different batches, thus arguably will exhibit different properties due to sensitivity to fabrication conditions.

Open-circuit voltage sensing experiments were conducted as described above and results for 3D-printed sub-mm eIPMC are shown in figure 11. Similar to what observed for inkjet printed eIPMC samples, the enhancement in sensing voltage is readily apparent between the control and eIPMC sensors and, in this case, even more dramatic. The FDM 3D-printed eIPMC sensors results show an approximately linear trend between increasing pressure and increasing open-circuit voltage, consistently with the proposed model. Through linear fitting, the open-circuit voltage versus pressure slope for the 3D-printed eIPMC samples 1 and 2 is approximately 107 and 122, respectively, when the intercept is fixed at 0. Similar to what noted in the discussion of inkjet printed sensors, the voltage output of the control IPMC does not show a clear trend and is significantly smaller for any value of the applied pressure.

A few comments are in order to interpret these results in terms of the modeling contributions of this paper. The presence of macro scale ridges such as the ones in figure 10 is expected to significantly modify the strain field that would develop in a conventional IPMC and create inhomogeneous strain through the thickness, as for example shown in figure 2. However, it should be noted that, differently from the representative case studied above via finite element analysis, the dimension $\tilde{d}$ of the ridges is very large with respect to the polymer semithickness, that is, $\tilde{d} \approx 0.6$ for the 3D-printed eIPMC sample 1 and $\tilde{d} \approx 0.2$ for the 3D-printed eIPMC sample 2. As such, two important differences arise from our simplified minimal mechanical and chemoelectromechanical model: (1) the dilatation field may be significantly affected in a region sufficiently far from the engineered electrode and (2) important chemoelectromechanical phenomena can actually occur within the polymer protrusion regions of the engineered electrode. These changes would call for at least a 2D fully coupled chemoelectromechanical analysis of the system which is significantly more complicated than our approach which aims at distilling the fundamental aspects of the problem. Furthermore, additional and possibly important effects that we have neglected (e.g. steric effects, composite layers, electrode surface roughness, chemoelectromechanical nonlinearities, non-rigid electrodes) may play a role in the response. Even though we do not hope to capture the correct value of γ from our minimal model, it is remarkable that an approximately linear behavior is observed, consistent with what has been predicted. At the first order, sample 2 (red curve) has relatively smaller polymer features and, arguably, a larger metal volume fraction at the interface region, than sample 2. Based on this observation, we would indeed expect that the slope for the linear fit of sample 2 should be larger than that of sample 1, consistently with our modeling efforts.

It is more difficult to capture the behavior of the absolute values of the voltage output for samples 1 and 2, especially when comparing between the low ($<0.7 \times 10^{-4}$) and high ($>0.7 \times 10^{-4}$) normalized pressure regions. This is presumably correlated to the detailed geometrical aspects of the interface. Therefore, especially in the absence of a more detailed mechanical model, we base our discussion on qualitative arguments. We predict that the more asymmetry is produced in the dilation at the electrodes, the higher the voltage response will be for a given pressure. The qualitative difference between the response of sample 1 and 2 could be explained by noticing that the sub-mm ridges in sample 2 have shorter spatial periodicity and smaller amplitude than those in sample 1. For a small applied pressure, especially given the fact that the eIPMC samples are compressed between parallel plates, sample 2 would contract in an almost homogeneous fashion, not too dissimilar from the control sample. Larger wavelength and larger amplitudes of the ridge would instead cause significant asymmetry in the sample 1. Vice versa, for large values of the pressure, the polymer deformation could possibly better follow the shape of the (non-rigid) electrode and yield an enhanced voltage output. The existence of a possibly critical pressure,

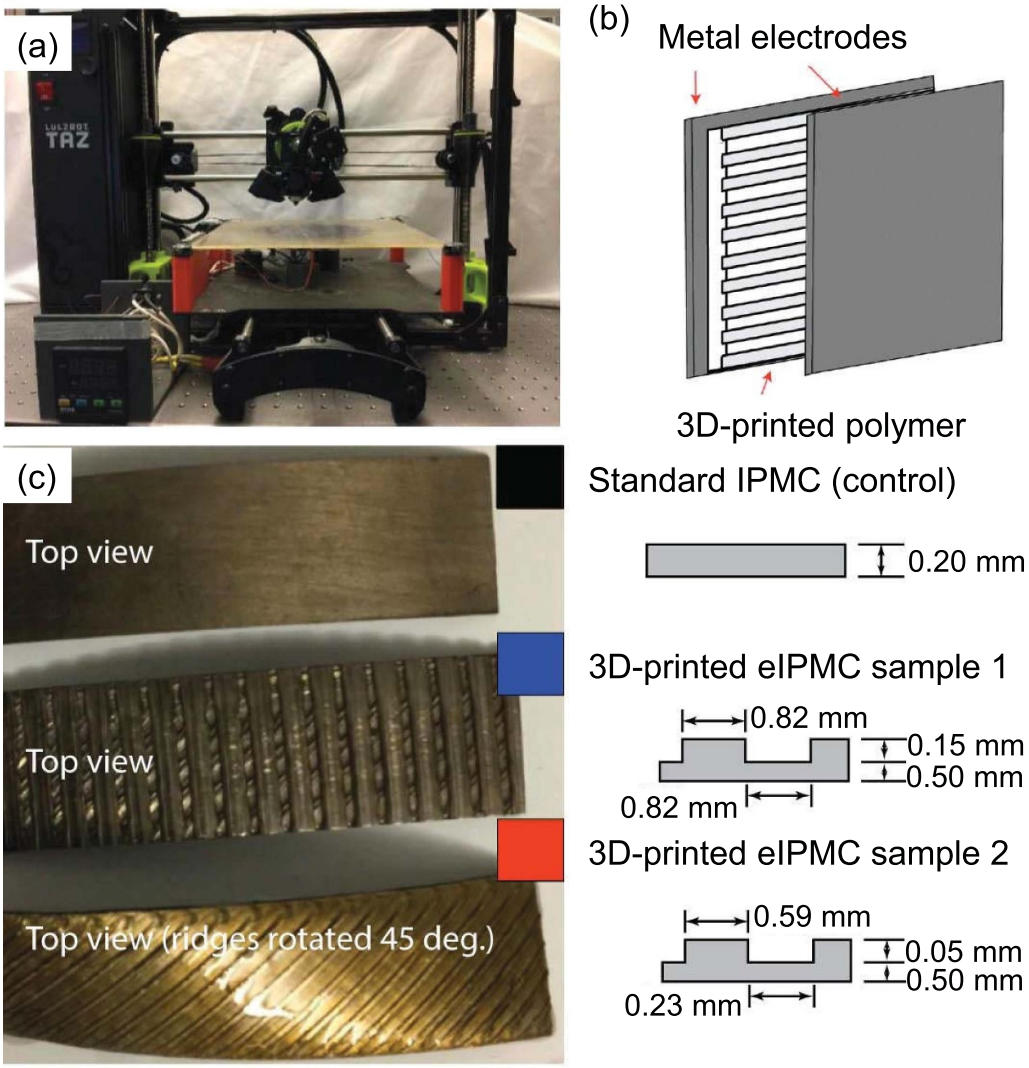

Figure 10. Sample eIPMCs fabricated using FDM 3D-printing process: (a) custom-designed IPMC 3D printer; (b) basic structure of 3D-printed eIPMC sensor with 3D-printed polymer membrane sandwiched between two platinum metal electrodes; and (c) control and two sub-mm eIPMC samples, along with dimensions of features created for testing. The sizes of the samples were approximately 9.5 mm × 31 mm.

for the geometry under study, is evidenced by the jump around $\hat{p} = 0.8 \times 10^{-4}$. Finally, the response of the control sample should be identically null, according to equation (13). However, small, uncontrollable differences between the electrode morphology cause mechanical asymmetry and a non-zero, albeit erratic, response.

4.2. Stencil printed eIPMCs

A second alternative sub-mm manufacturing approach is investigated to create printed eIPMC microfeatures on a pre-existing Nafion membrane, but with dramatically reduced manufacturing cost and processing time as compared to the inkjet printing studies. This approach is inspired by previous research involving the spray printing of Nafion dispersion to create custom IPMC membranes [25]. An immediate advantage of this approach is that higher concentration Nafion dispersions can be used during processing with inexpensive stencils, as compared to the manufacturer prescriptions for inkjet printer ink.

Therefore, a concentrated 20% weight Nafion dispersion, in its pure form, consisting of 20% weight D521 alcohol-based Nafion dispersion and propyl alcohol was used. The ink concentration of 1:4 (vol/vol) was optimized based on the required surface tension (28–42 g s^{-2}) and viscosity (10–12 mPa · s) and used to increase the amount of Nafion material deposited on the surface of the membrane per individual droplet.

The first step in the stencil printing process was to manufacture usable stencils to fabricate each eIPMC microfeature pattern. To do so, a 50 W Helix Laser Cutter was used to cut stencils from a Kapton adhesive backed sheet using a designated CAD file that specified the geometric pattern of each stencil.

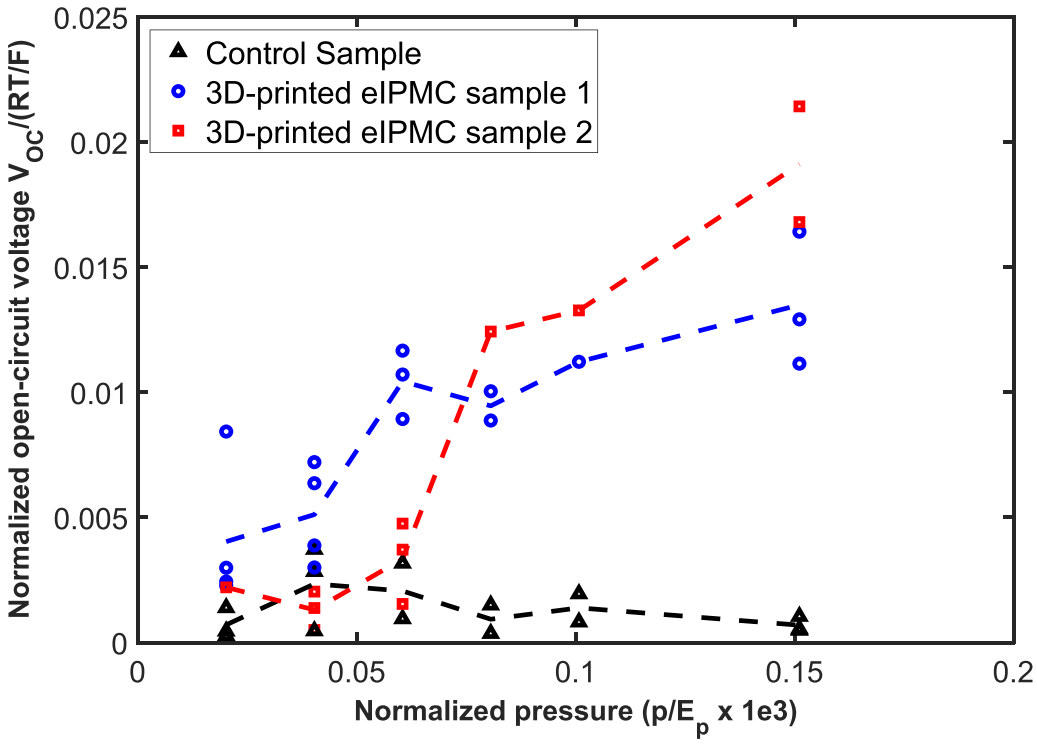

Figure 11. Measured normalized open-circuit voltage versus normalized applied pressure for FDM 3D-printed eIPMC sensors and control samples. Dashed lines pass through average values of the available measurements (markers).

Raster cutting conditions were implemented with 600 dpi cut settings. The same laser power and speed settings of 50% and 35% are used for each stencil to ensure the generation of consistent feature diameters. In each stencil, the spacing between microfeatures was varied to produce three stencils for testing. The stencils, designated as S_1, S_2, and S_3, have same feature diameter of 0.05 mm and feature interspacing dimensions of 0.6 mm, 0.7 mm, and 0.8 mm, respectively. Each pattern consisted of the same $10 \times 10\,\text{mm}^2$ outer pattern dimensions as the inkjet-printed samples to make the same final size eIPMC sensors. It should be noted that the actual cut feature diameters were larger than the specified dimensions in the CAD files due to the limitations of the laser cutter and beam width, leading to effective feature diameter of 0.3 mm. After the stencils were cut, they were repeatedly washed in ultrasonic baths with ethanol to remove the char debris from the inner edges of the stencil features.

The stencil-printed eIPMC samples were then fabricated by creating Nafion microfeatures on the surface of the same Nafion 117 membranes used for the previous experiments. The size membranes are similar to those for the inkjet printing samples. To do so, the Nafion membranes were placed on a clean glass slide with the Kapton stencil securely fastened to the top of the membrane. Each edge of the stencil was covered with 3 M adhesive tape to ensure that the deposited Nafion dispersion only contacted the membrane in the open areas of the stencil features.

The 20% weight pure Nafion dispersion was deposited on the surface of the membrane and stencil using a manual drop syringe. One drop was generously applied and the fluid was then manually dispersed over the entire surface of the stencil using a razor blade to ensure an even coating. A double coating of dispersion deposition was applied for each sample with 15 s of drying time in between each application. The excess dispersion was removed from the top layer of the stencil after each deposition to ensure that the features consistently dried to the height of the Kapton tape, which has a reported thickness 50.2 μm. The stencil was then immediately peeled from the Nafion membrane at a 45 degree angle to ensure that the features did not adhere to the stencil upon removal. Representative stencils, printed membranes, and eIPMC samples fabricated with this process are shown in figure 12.

Results of the open-circuit voltage sensing compression tests for the stencil-printed eIPMC samples are shown in figure 13. Sample S_1 and S_2 showed a marked increase in normalized voltage output. All samples S_1, S_2, and S_3 showed increased output response as the normalized pressure increased. Specifically, for the largest applied pressure reported, the normalized voltage output increased of 50%, 43.5%, and 20.7% in comparison to the control, respectively. In addition, it is interesting to note that the control sample does not show a monotonic increasing trend in the response. These results suggest that the sample with the largest number of printed features (leading to more pronounced asymmetry between the two electrode regions) shows the largest amount of sensing improvement.

However, in comparison to the inkjet-printed sample, the stencil-printed eIPMCs showed slightly weaker output. This is mainly attributed to the fact that there are significantly fewer microfeatures on the interfaces of the stencil printed

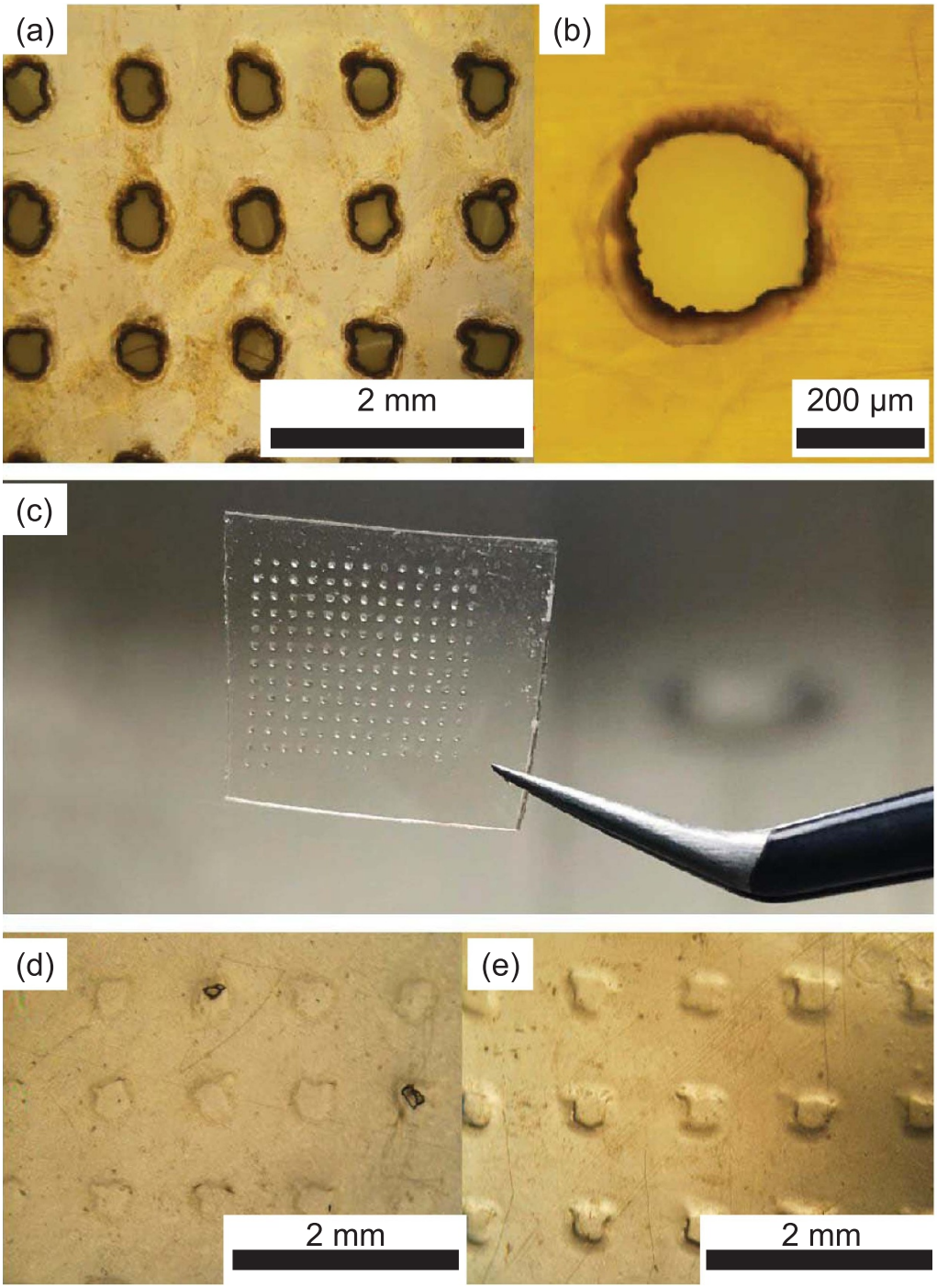

Figure 12. (a) OM image of S_3 sample stencil at 4× magnification (b) OM image of S_3 sample stencil at 20× magnification (c) example of a fresh stencil-printed eIPMC membrane with visible microfeature deposition (d) OM images of Sample S_3 at 4× magnification before plating with minimal signs of char debris inclusions in the stencil-printed features (e) OM images of Sample S_3 at 4× magnification after plating with indications of good surface and feature integrity.

samples. The difference can also be explained by the ascribed asymmetry caused by uncontrollable electrode morphology obtained from the different electroding batches. This fact further corroborates the huge variability in IPMC behavior that is dependent on the uncontrollable fabrication conditions present in the ECR process.

We conclude this discussion by observing that we believe that the new stencil printing method can be of great tutorial value, as it can be easily adopted by IPMC researchers to fabricate and start experimenting with eIPMCs without having to employ highly specialized equipment.

5. Remarks

The results on open-circuit voltage response for compression sensing in eIPMCs are the first of their kind and show the

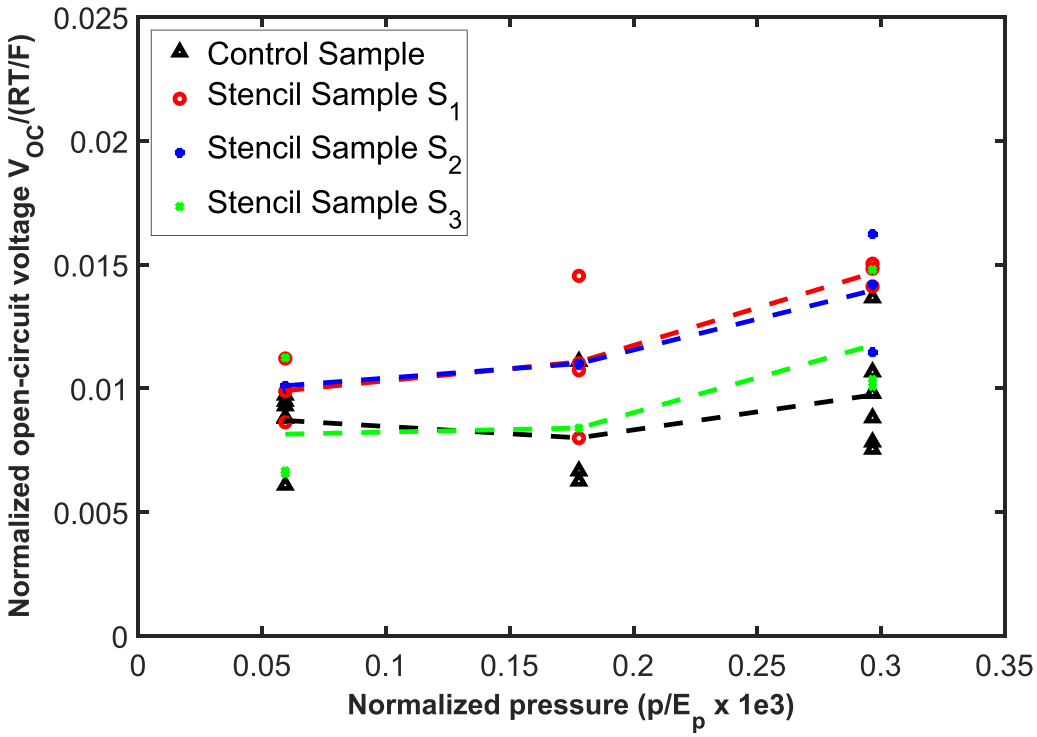

Figure 13. Normalized open-circuit voltage output of the stencil-printed eIPMC S_1, S_2, and S_3 samples compared to the standard IPMC control. Dashed lines pass through average values of the available measurements (markers).

potential for enhanced sensing capabilities through engineered interfaces. Remarkably, the proposed minimal model captures the essence of the structure-property relationships to demonstrate enhanced strain sensing performance.

We would like to remark that, as this is the first study on eIPMCs, we do not have a 'commercial-grade' sensor yet. A full optimization and characterization of the sensor is outside the scope of the current paper whose goal is to explore the mechanisms of compression sensing in eIPMCs. We note that the maximum allowable pressure and detection range may also depend on the particular kind of eIPMC, microscale or sub-mm scale featured sensor. In addition, the issue of repeatability and life of the sensor under cyclic loading is still to be fully addressed. As remarked, a more robust implementation of our sensors is needed, along with an optimized fabrication process and microstructural feature distribution. This is the object of current studies in preparation, including with the use of different advanced manufacturing technologies.

One last comment should be briefly directed to the comparison of the control response in figures 9, 11, and 13, in which, the result of FDM 3D printing is almost an order of magnitude larger than other methods. The only evident explanation for this behavior can be once again ascribed to asymmetry caused by uncontrollable electrode surface roughness. Note here that the Nafion membrane in the control sample of figure 11 was not sandblasted before plating [18] to preserve the inkjet printed microfeatures. This is yet another datapoint corroborating the huge variability in IPMC behavior dependent on uncontrollable fabrication conditions. We believe that 3D-printing and advanced manufacturing techniques of ionomer membranes with engineered properties will alleviate this problem in the future.

6. Conclusions

In this paper, we presented the design of tailored 3D-structured (engineered) polymer-metal interfaces to create enhanced eIPMC sensors with superior performance. Differently than traditional IPMC sensors in bending modes, these sensors are designed for operation in compression mode. A physics-based minimal chemoelectromechanical model is developed to predict the performance of the eIPMC sensor. The model incorporates structure microfeature effects, including microscale feature thickness, size, and spacing, that are translated into inhomogeneous volume change, or dilatation, in response to applied mechanical pressure. The dilatation is thus used as input in an analytically tractable chemoelectromechanical model that captures the essential physics of the problem and provides insight into the behavior of the sensor under open- and short-circuit conditions.

Three novel experimental approaches were described to create functional samples of eIPMC sensors using inkjet printing for microscale features, and fused deposition manufacturing and stencil printing techniques for sub-mm features. Experimental results were presented to show enhancement in electrochemical properties and in compression sensing capabilities compared to traditional sensors fabricated from sheet-form IPMC material and the effectiveness of the minimal model to interpret and explain the observed sensor behavior.

Future work will be devoted to advancing the manufacturing and modeling techniques proposed in this work and towards the integration of eIPMC sensor in mechatronics and cyber-physical systems.

Data availability statement

The data that support the findings of this study are available upon reasonable request from the authors.

Acknowledgments

This research was supported, in part, by the National Science Foundation under Grants 1809852, 1809455, and 1545857. Rebecca Histed was supported by a National Science Foundation Graduate Research Fellowship Program Grant number 1937966. Chantel K Lapins was supported through the REU program associated with NSF Grant number 1830958. Any opinions, findings, and conclusions or recommendations expressed in this material are those of the authors and do not necessarily reflect the views of the sponsor.

ORCID iDs

Kam K Leang https://orcid.org/0000-0003-1189-1673
Matteo Aureli https://orcid.org/0000-0003-4242-0081

References

[1] Patel S, Park H, Bonato P, Chan L and Rodgers M 2012 A review of wearable sensors and systems with application in rehabilitation *J. Neuroeng. Rehabil.* **9** 21
[2] Amjadi M, Kyung K-U, Park I and Sitti M 2016 Stretchable, skin-mountable and wearable strain sensors and their potential applications: a review *Adv. Funct. Mater.* **26** 1678–98
[3] Safari A and Akdogan E K (eds) 2008 *Piezoelectric and Acoustic Materials for Transducer Applications* 1 edn (Boston, MA: Springer) (https://doi.org/10.1007/978-0-387-76540-2)
[4] Fan F R, Tang W and Wang Z L 2016 Flexible nanogenerators for energy harvesting and self-powered electronics *Adv. Mater.* **28** 4283–305
[5] Shahinpoor M (ed) 2015 *Ionic Polymer Metal Composites (IPMCs): Smart Multi-Functional Materials and Artificial Muscles* (Cambridge, UK: Royal Society of Chemistry) (https://doi.org/10.1039/9781782622581)
[6] Oguro K, Asaka K and Takenaka H 1993 US Patent 5,268,082: Actuator element
[7] Shahinpoor M, Adolf D, Segalman D, and Witkowski W 1993 US Patent 5,250,167: Electrically controlled polymeric gel actuators
[8] Shahinpoor M and Mojarrad M 2000 US Patent 6,109,852: Soft actuators and artificial muscles
[9] Aureli M and Porfiri M 2013 Nonlinear sensing of ionic polymer metal composites *Contin. Mech. Thermodyn.* **25** 273–310
[10] Aureli M, Prince C, Porfiri M and Peterson S D 2010 Energy harvesting from base excitation of ionic polymer metal composites in fluid environments *Smart Mater. Struct.* **19** 015003
[11] Farinholt K and Leo D J 2004 Modelling of electromechanical charge sensing in ionic polymer transducers *Mech. Mater.* **36** 421–33
[12] Biddiss E and Chau T 2006 Electroactive polymeric sensors in hand prostheses: bending response of an ionic polymer metal composite *Med. Eng. Phys.* **28** 568–78
[13] Pugal D, Jung K, Aabloo A and Kim K J 2010 Ionic polymer-metal composite mechanoelectrical transduction: review and perspectives *Polymer Int.* **59** 279–89
[14] Bahramzadeh Y and Shahinpoor M 2011 Dynamic curvature sensing employing ionic-polymer-metal composite sensors *Smart Mater. Struct.* **20** 094011
[15] Farinholt K M, Pedrazas N A, Schluneker D M, Burt D W and Farrar C R 2009 An energy harvesting comparison of piezoelectric and ionically conductive polymers *J. Intell. Mater. Syst. Struct.* **20** 633–42
[16] Giacomello A and Porfiri M 2011 Underwater energy harvesting from a heavy flag hosting ionic polymer metal composites *J. Appl. Phys.* **109** 084903
[17] Cha Y, Verotti M, Walcott H, Peterson S D and Porfiri M 2013 Energy harvesting from the tail beating of a carangiform swimmer using ionic polymer metal composites *Bioinspir. Biomim.* **8** 036003
[18] Aureli M, Lin W and Porfiri M 2009 On the capacitance-boost of ionic polymer metal composites due to electroless plating: Theory and experiments *J. Appl. Phys.* **105** 104911
[19] Zangrilli U and Weiland L M 2011 Prediction of the ionic polymer transducer sensing of shear loading *Smart Mater. Struct.* **20** 094013
[20] Kocer B, Zangrilli U, Akle B and Weiland L 2015 Experimental and theoretical investigation of ionic polymer transducers in shear sensing *J. Intell. Mater. Syst. Struct.* **15** 2042–54
[21] Kocer B 2014 Experimental study of ionic polymer metal transducers characterization of transient response in sensing *PhD Thesis* University of Pittsburgh, Swanson School of Engineering, USA
[22] Volpini V, Bardella L, Rodella A, Cha Y and Porfiri M 2017 Modelling compression sensing in ionic polymer metal composites *Smart Mater. Struct.* **26** 035030
[23] Zhu Z, He X, He Q, Fang X, Hu Q and Chen H 2019 Ionic polymer pressure sensor with gradient shape based on ion migration *J. Appl. Phys.* **125** 024901
[24] Carrico J D, Traeden N W, Aureli M and Leang K K 2015 Fused filament 3D printing of ionic polymer-metal composites (IPMCs) *Smart Mater. Struct.* **24** 125021
[25] Trabia S 2018 Comprehensive Study of Spray-Painting and 3D Printing Fabrication Methods for Nafion® and Nafion® Equivalents in Ionic Polymer-Metal Composite Actuators and Sensors *PhD Thesis* Department of Mechanical Engineering, University of Nevada, Las Vegas, USA
[26] Porfiri M 2009 Influence of electrode surface roughness and steric effects on the nonlinear electromechanical behavior of ionic polymer metal composites *Phys. Rev.* E **79** 041503
[27] Cha Y, Aureli M and Porfiri M 2012 A physics-based model of the electrical impedance of ionic polymer metal composites *J. Appl. Phys.* **111** 124901
[28] Aureli M and Porfiri M 2012 Effect of electrode surface roughness on the electrical impedance of ionic polymer metal composites *Smart Mater. Struct.* **21** 105030
[29] Torquato S 2002 *Random Heterogenous Materials* (New York, NY: Springer)
[30] Christensen R M 1991 *Mechanics of Composite Materials* (Malabar, FL: Krieger Publishing Company)
[31] Cha Y and Porfiri M 2014 Mechanics and electrochemistry of ionic polymer metal composites *J. Mech. Phys. Solids* **71** 156–78
[32] Porfiri M 2019 Sensing mechanical deformation via ionic polymer metal composites: a primer *IEEE Instrum. Meas. Mag.* **22** 5–12

[33] Porfiri M 2008 Charge dynamics in ionic polymer metal composites *J. Appl. Phys.* **104** 104915
[34] Nayfeh A H 1981 *Introduction to Perturbation Techniques* (New York, NY: Wiley-Interscience)
[35] Soltman D and Subramanian V 2008 Inkjet-printed line morphologies and temperature control of the coffee ring effect *Langmuir* **24** 2224–31
[36] Asaka K, Kruusamae K, Kim K J, Palmre V and Leang K K 2016 *IPMCs as EAPs: How to Start Experimenting With Them* (Springer Int. Publishing AG) (https://doi.org/10.1007/978-3-319-31530-0_10)
[37] Bard A J and Faulkner L R 2001 *Electrochemical Methods: Fundamentals and Applications* (Hoboken, NJ: Wiley)
[38] Volpini V and Bardella L 2021 Asymptotic analysis of compression sensing in ionic polymer metal composites: the role of interphase regions with variable properties *Math. Eng.* **3** 1–31
[39] Zhu Z, Chang L, Asaka K, Wang Y, Chen H, Zhao H and Li D 2014 Comparative experimental investigation on the actuation mechanisms of ionic polymer-metal composites with different backbones and water contents *J. Appl. Phys.* **115** 124903
[40] Nemat-Nasser S and Wu Y 2003 Comparative experimental study of ionic polymer-metal composites with different backbone ionomers and in various cation forms *J. Appl. Phys.* **93** 5255–67